Permanent Set of Cross-Linking Networks: Comparison of Theory with Molecular Dynamics Simulations

Dana R. Rottach,[†] John G. Curro,*[,†,‡] Joanne Budzien,[‡] Gary S. Grest,[‡] Carsten Svaneborg,[§] and Ralf Everaers[§]

Department of Chemical and Nuclear Engineering, University of New Mexico, Albuquerque, New Mexico 87131, Sandia National Laboratories, Albuquerque, New Mexico 87185, and Max Planck Institut für Physik Komplexer Systeme, Nöthnitzer Strasse 38, 01187 Dresden, Germany

Received April 4, 2006

ABSTRACT: The permanent set of cross-linking networks is studied by molecular dynamics. The uniaxial stress for a bead−spring polymer network is investigated as a function of strain and cross-link density history, where cross-links are introduced in unstrained and strained networks. The permanent set is found from the strain of the network after it returns to the state-of-ease where the stress is zero. The permanent set simulations are compared with theory using the independent network hypothesis, together with the various theoretical rubber elasticity theories: affine, phantom, constrained junction, slip-tube, and double-tube models. The slip-tube and double-tube models, which incorporate entanglement effects, are found to be in very good agreement with the simulations.

1. Introduction

Stress relaxation and aging in strained polymer networks can be attributed to two distinct processes. At short times, relaxation is dominated by viscoelastic effects, in which chains approach a new equilibrium state through diffusive processes. The dominant effect at long times is stress relaxation occurring as a result of chemical changes, such as chain scission and additional cross-linking, that affect the network structure.[1,2] The network connectivity is altered as the polymer chains break and reform. Chemical reaction can occur in most organic polymer networks at high temperatures and/or long times. The permanent changes in the connectivity of the networks have attendant changes in the elastic properties with time. On very long time scales, the kinetics of the various chemical reactions, rather than the diffusive relaxation, controls the time dependence of the macroscopic properties.[1,2]

Tobolsky was the first to systematically study these *chemical relaxation* effects.[3,4] Fundamentally different behavior results depending upon whether chemically induced chain scission or cross-linking occurs. Chemical scission of bonds causes the effective cross-link density of the network, and therefore the equilibrium rubber elastic modulus, to decrease with time. Neglecting viscoelastic effects, the stress on a network undergoing only scission reactions depends on the current value of the cross-link density. By contrast, the stress on a network with additional cross-linking (e.g., postcuring) depends not only on the current value of the cross-link density but also on the state of strain the sample was in when each cross-link formed. Tobolsky[3,5] and co-workers conjectured that an elastomer, postcured in a strained state, could be analyzed with a *two-network* model consisting of distinct networks cross-linked in the unstrained and strained states. This model was later studied by Berry, Scanlan, and Watson[6,7] and compared with experiments on rubber networks. In a classic paper, Flory[8] generalized the two-network model to an independent network model in which a network is cross-linked in a series of arbitrary strained states or *stages*. Flory rigorously demonstrated that an affine, Gaussian network undergoing cross-linking is equivalent to a collection of independent networks. Each network (or stage) corresponds to its zero stress state and has a cross-link density resulting from cross-links introduced at each stage of the strain history. Flory[8] went on to consider the consequences of scission of cross-links formed in previous stages. Fricker[9] later showed similar behavior for phantom, Gaussian networks. More recently the independent network hypothesis has been used in general constitutive models by Wineman[10−12] and co-workers and has been tested in various experiments[13,14] on elastomeric networks.

In a recent paper, some of us presented[15] molecular dynamics (MD) simulations for bead−spring polymer networks undergoing cross-linking reactions in unstrained and uniaxially strained states. By examining the stress in the strained state, we found that the independent network hypothesis provided a very accurate description of the postcured network. In this previous investigation,[15] it was shown that postcured networks exhibited a permanent set when the uniaxial stress was returned to zero. The purpose of the present investigation is to study the permanent set of cross-linking networks in more detail and to compare our MD simulations with theoretical predictions. In this work we extracted the permanent set from MD simulations of bead−spring polymer networks, taking particular care to achieve equilibrium conditions.

Molecular dynamics simulations on nonreacting bead−spring polymer networks have been used by Everaers and co-workers[16−18] to test various rubber elasticity models and by Grest et al.[19−21] to study gelation and viscoelasticity. Molecular dynamics simulations are a particularly powerful tool to study chemically reacting polymer networks because it is difficult to carry out well-controlled chemical relaxation experiments on elastomeric networks in the laboratory. Molecular dynamics simulation enables precise control over the chemistry. For example, scission and cross-linking can be selectively turned on and off in the simulation, whereas this

* Author to whom correspondence should be addressed. E-mail: jgcurro@sandia.gov.
[†] University of New Mexico.
[‡] Sandia National Laboratories.
[§] Max Planck Institut für Physik Komplexer Systeme.

10.1021/ma060767x CCC: $33.50
Published on Web 07/15/2006

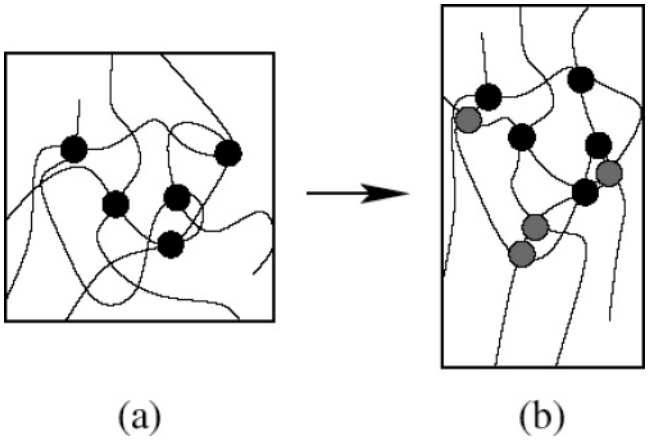

Figure 1. Schematic depiction of the cross-linking/strain history of simulated networks (two-stage networks). Left panel: A network is formed from a melt of linear polymer chains in the isotropic, unstrained state by the addition of cross-links (represented here by black circles). Right panel: The network is uniaxially deformed at constant volume, and new cross-links (gray circles) are added.

is difficult to achieve in the laboratory. Moreover, because networks are infusible and insoluble (although they will undergo solvent swelling), standard analytical techniques to characterize network structure caused by chemical reaction can be difficult to apply. The characterization tools available for studying the network connectivity in the laboratory are difficult to use and offer less than ideal characterization. Indeed, the stress relaxation behavior itself might be the most sensitive measure of any chemically induced changes in network structure.

Permanent set is commonly used in the rubber industry as an indicator of the resistance of an elastomeric material to chemical aging. To better understand the relation between the permanent set and the combined effects of the cross-link density and strain history of a network, we compared our predictions from MD simulations to predictions from various rubber elasticity theories, utilizing the independent network hypothesis. In particular we investigated the following theories: (1) the affine model,[22] (2) the phantom model of James and Guth,[23] (3) the constrained junction theory,[24,25] (4) the slip-tube model of Rubinstein and Panyukov,[26] and (5) the double-tube model of Everaers.[27,28] In section 2 we describe our MD simulation methodology. In section 3 we employ the independent network hypothesis, together with the various rubber elasticity theories, to compute the permanent set. In section 4 we discuss the detailed comparisons between simulation and theory.

2. Molecular Dynamics Simulations

In this work we employed MD simulations[29] to study the effects of cross-linking in a uniaxial strained state on the permanent set of a network. Our simulations are conceptually similar to the laboratory experiment where a sample is: (i) cross-linked at zero strain (stage 1), (ii) elongated at constant volume to a stretch ratio of λ_2 where additional cross-links are introduced (stage 2), and then (iii) released to its new state-of-ease λ_s at zero stress. A schematic of our network simulation is shown in Figure 1. We form a network in an initial unstrained, isotropic state, where sufficient cross-links are introduced to be well above the gel point. We then apply a uniaxial strain, at constant volume, and introduce additional cross-links. Here we use ν_1 and ν_2 to denote the number density of network chains (twice the cross-link density) introduced at stages 1 and 2, respectively.

The polymers were modeled using the standard bead−spring model[20] in which the beads interact with a truncated Lennard-Jones potential

$$V(r) = 4\epsilon\left(\left(\frac{\sigma_{LJ}}{r}\right)^{12} - \left(\frac{\sigma_{LJ}}{r}\right)^{6} + \frac{1}{4}\right) \quad r \le 2^{1/6}\sigma_{LJ}$$
$$= 0 \quad r > 2^{1/6}\sigma_{LJ} \tag{1}$$

where σ_{LJ} and ϵ are the Lennard-Jones parameters. Additional interaction is added between bonded sites, either along the original chain or between cross-linked sites

$$V_{FENE}(r) = -\frac{k}{2}R_0^2 \ln(1 - (r/R_0)^2) \quad r \le R_0$$
$$= \infty \quad r > R_0 \tag{2}$$

where $R_0 = 1.5\sigma_{LJ}$ and $k = 30\epsilon/\sigma_{LJ}^2$. Large-scale, MD simulations were performed in a NVT ensemble using the LAMMPS parallel MD code,[29] modified to incorporate chemical reactions.[15] The simulations typically were run employing between 8 and 36 processors, with individual runs using approximately 1700 processor hours/million time steps. The molecular dynamics time step was 0.01τ where $\tau = \sigma_{LJ}\sqrt{m/\epsilon}$ and m is the mass of a bead. Periodic boundary conditions were employed with a density $\rho\sigma_{LJ}^3 = 0.85$ and reduced temperature $k_BT/\epsilon = 1$. Two sets of simulations denoted as A and B, differing in the way cross-links are introduced, were carried out.

For simulation set A, the melt consisted of 500 chains of 500 sites each. Four percent of the sites on each chain were randomly designated as reactive, subject to the condition that pairs of reactive sites were separated by at least two bonds. The system was equilibrated before any reactions were performed. The reaction phase consisted of evaluating the distances between all pairs of reactive sites at regular time intervals. Pairs of sites within a capture radius of $1.3\sigma_{LJ}$ had a probability q of becoming bonded. The time interval and q were adjusted so that quasi-equilibrium conditions were maintained. The cross-linking reactions exhibited second-order kinetics for conversions less than $p = 0.6$ (number of sites reacted divided by the total number of reactive sites).[15] A conversion of $p = 0.6$ was achieved in approximately 600τ (or 60 000 MD time steps). Cross-linking reactions became diffusion-controlled at larger extents of conversion. A conversion of approximately $p_{gel} = 0.096$ ($\nu_{gel} = 0.00326/\sigma_{LJ}^3$) corresponds to the gel point. Samples were cross-linked to conversions $p = 0.2$, 0.4, and 0.6. This gives average degrees of polymerization between chemical cross-links of 125, 62.5, and 41.7 sites (or $\nu_1 = 0.0068$, 0.0136, and $0.0204/\sigma_{LJ}^3$), respectively.

Simulation set B was carried out starting with 80 chains of 3500 monomers. By contrast with simulations A, the cross-links in simulations B were introduced in a single step. The melt of chains was equilibrated in the unstrained state as in simulations A, after which 1400 randomly chosen pairs of sites within a capture radius of $1.3\sigma_{LJ}$ were cross-linked instantaneously. This corresponds to an average degree of polymerization between cross-links of 100 monomers or $\nu_1 = 0.0085/\sigma_{LJ}^3$. Because the chains are much longer in simulation B than A, the gel point occurs at lower conversions. We estimate for simulations B that[19] $\nu_{gel} = 0.00029/\sigma_{LJ}^3$.

Both sets of simulations start with a cubic, periodic box with sides L_0 in the unstrained state. The network is uniaxially deformed at constant volume by changing the box length to λL_0 in the x direction and to $L_0/\sqrt{\lambda}$ in the y and z directions.[15]

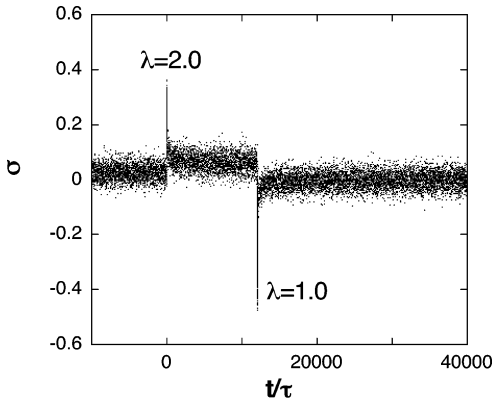

Figure 2. Stress history for simulation A with a fixed number of stage 1 cross-links $\nu_1 - \nu_{gel} = 0.0171/\sigma_{LJ}^3$. The system first is uniaxially stretched to $\lambda = 2.0$ at $t/\tau = 0$ and then allowed to relax. The system is then compressed to its final value, here $\lambda = 1.0$. Note that the stress decays slowly with time after each deformation event.

Table 1. State-of-Ease and Permanent Set Results from MD Simulation Set A[a]

$\sigma_{LJ}^3(\nu_1 - \nu_{gel}) \times 10^3$	$\sigma_{LJ}^3 \nu_2 \times 10^3$	λ_2	λ_s	P_s
3.5	0	2	1.008	0.008
3.5	6.8	2	1.14	0.14
3.5	13.6	2	1.24	0.24
3.5	20.4	2	1.32	0.32
10.3	0	2	1.002	0.002
10.3	6.8	2	1.14	0.14
10.3	13.6	2	1.23	0.23
17.1	0	2	1.004	0.004
17.1	6.8	2	1.10	0.10

[a] 500 chains of 500 monomers.

This deformation is accomplished by a series of small affine deformations, $\Delta\lambda$, applied to the coordinates of each site, to give the transformation $\{x_i,y_i,z_i\} \rightarrow \{x_i\Delta\lambda, y_i\sqrt{\Delta\lambda}, z_i/\sqrt{\Delta\lambda}\}$ until the desired strain is achieved. No cross-linking is allowed to occur during the deformation in either simulations A or B. The molecular dynamics is continued during the deformation process, so that even though the microscopic steps are affine the network is allowed to adjust, and the overall deformation is nonaffine and volume-conserving. The average stress in the direction of strain is obtained[27] from the simulation as the deviatoric part of the stress tensor $\sigma_x = P_{xx} - P$ where $P = \sum_\alpha P_{\alpha\alpha}/3$ is the hydrostatic pressure and $P_{\alpha\beta}$ is the stress tensor. The true stress for these incompressible systems (with a Poisson's ratio of 1/2) is $\sigma = (3/2)\sigma_x$. Figure 2 shows the recorded true stress in a typical simulation where a network of fixed cross-link density is uniaxially stretched to $\lambda = 2.0$, allowed to relax for a period of time, and then compressed to its original strain $\lambda = 1.0$. Note that stress relaxation occurs after each deformation. We typically ran the simulations for $10^5\tau$ and averaged the stress over the last $3-5 \times 10^4\tau$.

After the networks were deformed to an extension ratio of λ_2, additional cross-links were then added to the networks while in the strained state. For simulations A, the system was equilibrated for approximately $2 \times 10^4\tau$ after which the stage 2 cross-links were added gradually at the same rate as in stage 1. In simulations B the stage 2 cross-links were added immediately after deformation. After the second stage cross-links were introduced, both networks A and B were equilibrated for $10^5\tau$. In this manner, we obtained a series of networks with various first and second stage network chain densities ν_1 and ν_2 shown in Tables 1 and 2. Even though simulation sets A and B differ in the way the cross-links were introduced and the dynamics would certainly be different, we expect that the equilibrium behavior would be similar for both the A and the B networks.

Table 2. State-of-Ease and Permanent Set Results from MD Simulation Set B[a]

$\sigma_{LJ}^3(\nu_1 - \nu_{gel}) \times 10^3$	$\sigma_{LJ}^3 \nu_2 \times 10^3$	λ_2	λ_s	P_s
8.21	0	2.0	1.01	0.01
8.21	4.25	2.0	1.10	0.10
8.21	8.50	2.0	1.17	0.17
8.21	12.76	2.0	1.22	0.22
8.21	4.25	4.0	1.17	0.057
8.21	8.50	4.0	1.30	0.10

[a] 80 chains of 3500 monomers.

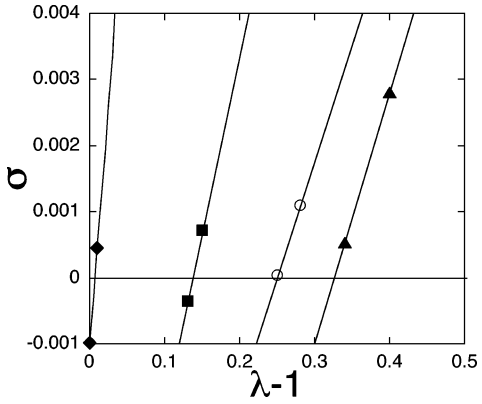

Figure 3. Permanent set determinations. Systems are equilibrated at strains near the expected state-of-ease, and straight line fits are used to determine the uniaxial deformation λ_s corresponding to zero stress. These various curves correspond to networks with $\nu_1 = 0.0068/\sigma_{LJ}^3$. Additional cross-links are then added in the strained state $\lambda_2 = 2$: $\nu_2 = 0$ (diamonds), $\nu_2 = 0.0068/\sigma_{LJ}^3$ (squares), $\nu_2 = 0.0136/\sigma_{LJ}^3$ (open circles), and $\nu_2 = 0.0204/\sigma_{LJ}^3$ (triangles). Note that when no additional cross-links are added in the strained state $\lambda_s \approx 1.01$.

The permanent set of a network is defined according to

$$P_s = \frac{\lambda_s - 1}{\lambda_2 - 1} \tag{3}$$

where λ_2 is the deformation ratio at which the stage 2 cross-links were added and λ_s is the deformation ratio to which the sample returns at its zero stress, state-of-ease. For complete recovery $P_s = 0$, while if there is no recovery of the sample $P_s = 1$. We found that λ_s could be more accurately determined from a series of constant strain simulations near the state-of-ease, instead of using a constant stress ensemble. λ_s was then found from interpolation as shown in Figure 3. In this figure we plotted the stress−strain curves for a series of networks having different extents of stage 2 cross-links introduced in the strained state. Note that for the case when no additional stage 2 cross-links are added (diamonds) the zero stress condition should be $\lambda_s = 1.0$. As can be seen from Figure 3, the actual state-of-ease measured was $\lambda_s \approx 1.01$. This difference (∼1%) is attributable to residual viscoelastic processes that have not completely relaxed. Thus we conclude that for samples equilibrated for greater than $10^5\tau$ we achieve the equilibrium state within the statistical error. On the basis of this result, all the simulations presented here have been equilibrated for at least $10^5\tau$. Permanent set results from MD simulations on networks A and B are presented in Tables 1 and 2, respectively.

The macroscopic network stresses associated with the determination of the permanent set were computed exactly from the MD simulations using the virial theorem for the stress tensor.

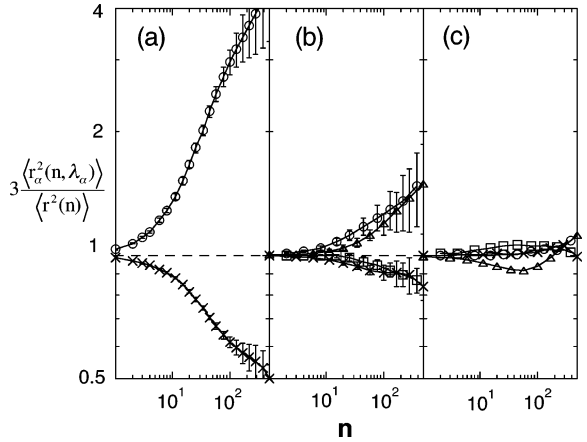

Figure 4. Comparison between microscopic deformations of stage 1 and stage 2 B networks with identical strain history: (a) $\lambda = 2$ before adding $\nu_2 = 0.0085/\sigma_{LJ}^3$ cross-links, (b) $\lambda = 1.17$ (i.e., the state-of-ease of the stage 2 network), and (c) $\lambda = 1.00$ (i.e., the state-of-ease of the stage 1 network). Symbols denote microdeformations parallel and perpendicular respectively to the strain direction for stage 1 (circles and ×'s) and stage 2 (triangles and squares) networks.

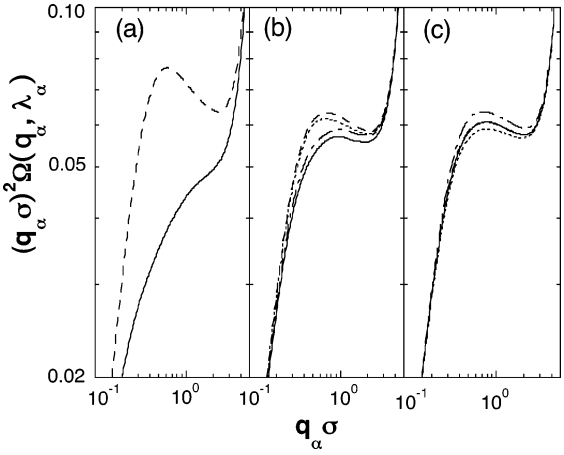

Figure 5. Comparison between microscopic chain conformations in stage 1 and 2 B networks as accessible through small-angle neutron scattering scattering experiments. We show a Kratky plot of the form factor $\Omega(q_\alpha,\lambda_\alpha)$ of labeled chains of length $N = 100$ for the same systems shown in Figure 4. Lines denote scattering parallel ($\alpha = ||$) and perpendicular ($\alpha = \perp$) to the strain direction for stage 1 (solid, dashed) and stage 2 (dash−dotted, dashed) networks.

It is also instructive to obtain the stress by considering the network mesoscopically as composed of ideal, entropic springs or segments, each consisting of n monomers. The density of segments is $\rho_s(n) = \rho/n$, where ρ is the monomer density. The entropic spring constant of a segment is $3k_BT/\langle r^2(n)\rangle$ where $\langle r^2(n)\rangle$ is the mean-square end-to-end distance of a segment of length n in the isotropic melt state before crosslinking. The mean-square end-to-end extensions of a segment in the directions parallel and perpendicular to the strain are denoted by $\langle r_{||}^2(n,\lambda_{||})\rangle$ and $\langle r_\perp^2(n,\lambda_\perp)\rangle$ respectively. Hence the length-scale-dependent (n-dependent) entropic stress can be expressed using only sampled mean-square extensions as[18]

$$\sigma(n,\lambda) = 3k_BT\rho_s(n)\left[\frac{\langle r_{||}^2(n,\lambda_{||})\rangle}{\langle r^2(n)\rangle} - \frac{\langle r_\perp^2(n,\lambda_\perp)\rangle}{\langle r^2(n)\rangle}\right] \qquad (4)$$

The macroscopic stress is obtained by extrapolating $\sigma(n,\lambda)$ to the limit $n \to 0$.

Figure 4 shows the microscopic deformations on different length scales (a) at λ_2, (b) after compression to λ_s, and (c) after further compression to $\lambda = 1$ for the B networks with and without adding additional cross-links. Regardless of the strain and cross-link history of the sample, the microscopic deformations at large length scales always converge to the macroscopic strain, indicating an affine strain response. At short distances, the chain conformations are only weakly affected by the macroscopic strain. This is a consequence of the local liquidlike behavior characteristic of polymer networks. The height of the gap between the parallel and the perpendicular microscopic deformations at short distances is directly related to the microscopic stress through eq 4. We observe the expected locally isotropic chain statistics for networks in their state-of-ease (stage 1 networks at $\lambda = 1$ in Figure 4c; stage 2 networks at $\lambda = \lambda_s$ in Figure 4b) as well as the inversion of local and global compression and elongation in stage 2 networks for $1 < \lambda < \lambda_s$. Qualitatively, the observed differences in the microscopic deformations between stage 1 and 2 networks agree with the independent network hypothesis and the idea of a compressive deformation of the second network created in the deformed state.

The characteristic inversion of compression and elongation on intermediate scales should be observable in small-angle neutron scattering experiments with a low fraction of labeled chains embedded into the network.[30] In Figure 5 we show a Kratky plot of the single-chain form factor for the same systems as in Figure 4 where we chose a labeling length $N_1 = 100$ equal to the average strand length of the stage 1 network. The plateau observed at intermediate length scales is due to the random walk statistics of the labeled chains, while the peak at short length scales (large q values) is due to the incoherent scattering contribution where $\Omega(q) = 1/N_1$. The alternative representation of the data in Figure 6 shows that one can extract qualitatively similar information from the approximately inverted form factors[31] as from the experimentally inaccessible mean-square internal distances shown in Figure 4. The apparently stronger microscopic deformations at short distances are due to non-Gaussian distance distribution functions.[31]

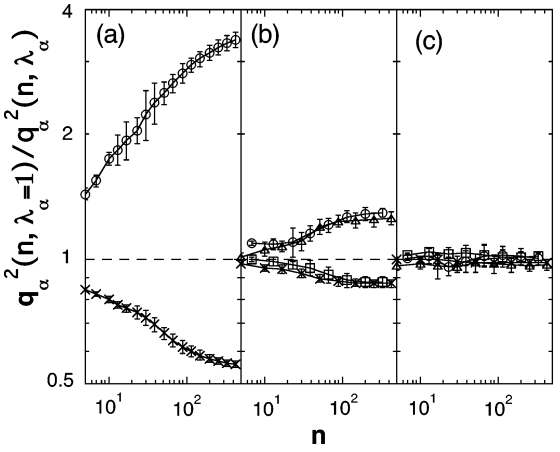

Figure 6. Alternative representation of the single-chain form factors shown in Figure 5 that qualitatively reproduces the directly sampled microscopic deformations shown in Figure 4. The idea[31] is to assign a typical wave vector q to a chemical distance n by solving $n \equiv \Omega(q(n))$. Plotting $q^2(n,\lambda_\alpha = 1)/q^2(n,\lambda_\alpha)$ yields information that is directly comparable to the ratios $3\langle r_\alpha^2(n,\lambda_\alpha)\rangle/\langle n^2(n)\rangle$ shown in Figure 4. Symbols are identical to those used in Figure 4.

Figure 7 shows the microscopic Gaussian stresses as a function of the length scale obtained from eq 4 and the data presented in Figure 4. They are in good agreement with the stress obtained from the virial tensor.[38] This suggests that to understand the microscopic origin of permanent set, the relevant observable to study from computer simulations is the length-

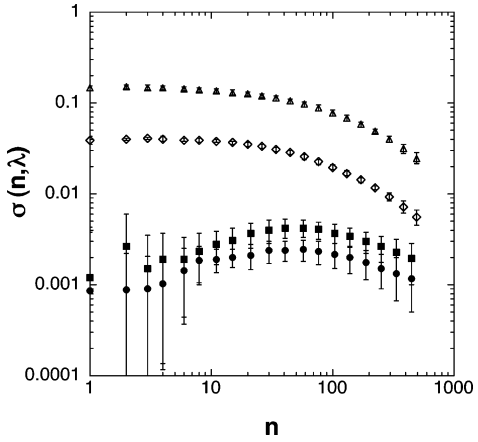

Figure 7. Entropic stress obtained from eq 4 as a function of the length scale *n*. The points were obtained from MD simulations of B networks with $\nu_2 = 0.0085/\sigma_{LJ}^3$ after cross-linking in the strained states $\lambda_2 = 2$ (diamonds and circles) and $\lambda_2 = 4$ (triangles and squares). The diamonds and triangles correspond to entropic stresses obtained in the strained states, and the circles and squares refer to the entropic stresses in the states of ease.

scale-dependent stress $\sigma(n,\lambda)$. Furthermore, the challenge for theory is to be able to predict the strain dependence of the microscopic deformations $3\langle r_{||}^2(n,\lambda_{||})\rangle/\langle r^2(n)\rangle$ and $3\langle r_{\perp}^2(n,\lambda_{\perp}\rangle/\langle r^2(n)\rangle$ based on the strain and cross-linking history of the network and precursor melt.

3. Theory

3.1. Independent Network Hypothesis. Tobolsky hypothesized[3−5] that a two-stage network can be thought of as two independent networks: a network of ν_1 chains/volume cross-linked in the unstrained state and a second network of ν_2 chains/volume cross-linked under strain. This is easily generalized to an arbitrary number of stages *n* where the strain energy W_n can be written in the form

$$W_n(\lambda_x,\lambda_y,\lambda_z) = \sum_{i=1}^{n} W\left(\frac{\lambda_x}{\lambda_{x,i}},\frac{\lambda_y}{\lambda_{y,i}},\frac{\lambda_z}{\lambda_{z,i}},\nu_i\right) \tag{5}$$

where *W* is the strain energy of a single network with fixed cross-link density, λ_x, λ_y, and λ_z are the principal stretch ratios, and $\lambda_{x,i}$, $\lambda_{y,i}$, and $\lambda_{z,i}$ are the corresponding principal stretch ratios at stage *i* when ν_i network chains are introduced. The principal stresses can then be found from $\sigma_x = \lambda_x \partial W_n/\partial\lambda_x$, etc. The independent network hypothesis implies that the uniaxial stress σ_n of an *n* stage network can be related to the uniaxial stretch ratio λ according to

$$\sigma_n(\lambda) = \sum_{i=1}^{n} \sigma(\lambda/\lambda_i,\nu_i) \tag{6}$$

where σ is the corresponding uniaxial stress for a nonreacting network having a fixed number of cross-links. Note that the independent network hypothesis in eq 6 is general and applicable to any constitutive model or rubber elasticity theory. Equation 6 was shown in ref 15 to be in excellent agreement with MD simulations for two-stage networks.

We can employ eq 6 to compute the state-of-ease λ_s and the permanent set by equating the stress to zero. For a two-stage network this leads to the condition

$$\sigma(\lambda_s,\nu_1) + \sigma(\lambda_s/\lambda_2,\nu_2) = 0 \tag{7}$$

where we have implicitly taken $\lambda_1 = 1$ as the unstrained state. Thus it can be seen that the permanent set can be computed from the independent network hypothesis, together with any rubber elasticity model for σ. In this investigation, we will use eq 7 to compute the permanent set from various rubber elasticity theories. The accuracy of the various theories is evaluated by comparison with the results from our MD simulations. Prediction of permanent set from rubber elasticity theories is particularly challenging since the zero stress state is determined from a balance between the stage 1 network in tension and the stage 2 network in compression. Some theories (e.g., Mooney−Rivlin equation) are accurate in tension but not in compression and hence will not be accurate in predicting permanent set.

3.2. Affine/Phantom Models. Most classical models of rubber elasticity treat an elastomeric material as a network of Gaussian chains. The most difficult aspect of the rubber elasticity problem involves making a connection between the microscopic configurations of the network chains and the macroscopic dimensions of the bulk system. The simplest and oldest approach is the affine model[32] of Wall and Flory[22] that fixes network junctions in an elastic continuum. The phantom model developed by James and Guth[23] allows junctions to fluctuate about their affine positions. The uniaxial true stress predicted for a network of chain density of ν at constant volume is given by

$$\sigma_{Ph}(\lambda) = \alpha\nu kT(\lambda^2 - \lambda^{-1}) \tag{8}$$

where α is a factor related to network connectivity, junction mobility, and network segment effectiveness. For tetrafunctional networks, $\alpha = 1$ for the affine model, and $\alpha = {}^1/_2$ for the phantom model. Network imperfections, such as intramolecular cycles and dangling ends, tend to reduce the magnitude of α. On the basis of these models, we define a shear modulus due to chemical cross-links as

$$G_c \equiv \alpha\nu kT \tag{9}$$

By explicitly treating the cross-linking process, Flory[8] and Fricker[9] demonstrated that the affine and phantom models, respectively, exactly obey the independent network hypothesis. Thus eqs 7 and 8 lead to the following relation for the state-of-ease, λ_s

$$\left(\lambda_s^2 - \frac{1}{\lambda_s}\right) + \left(\frac{\lambda_s^2}{\lambda_2^2} - \frac{\lambda_2}{\lambda_s}\right)\frac{\nu_2}{(\nu_1 - \nu_{gel})} = 0 \tag{10}$$

for both the affine and phantom models. In eq 10 ν_1 is the number of network chains/volume added in the unstrained state, and ν_2 is the number density of network chains added in the strained state λ_2. $\nu_1 - \nu_{gel}$ appears in the equation for λ_s in all the theoretical models because only cross-links added after the gel point contribute to the network elasticity. For this two-stage network eq 10 can be analytically solved for λ_s. Equation 3 can then be employed to obtain an analytical expression for the permanent set for the affine and phantom models

$$P_s = \frac{\lambda_2\left(\dfrac{\nu_2/(\nu_1 - \nu_{gel}) + 1/\lambda_2}{\nu_2/(\nu_1 - \nu_{gel}) + \lambda_2^2}\right)^{1/3} - 1}{\lambda_2 - 1} \tag{11}$$

Equation 11 was first deduced by Tobolsky.[3]

3.3. Constrained Junction Model. The classical models discussed above only include the effects of chemical cross-links. Due to the polymeric nature of the precursor chains, entangle-

ments may become trapped and contribute to the stress on the sample. The constrained junction model is based on the premise that the effect of entanglements is to restrict the fluctuations of the network junctions.[24,25,33−35] This constraint is expressed by a harmonic potential on each network junction centered at the affine junction position. A parameter κ varies the relative strengths of the constraints due to the entanglement term and the phantom connectivity term. The strain energy function for uniaxial tension is given by

$$W = \frac{\nu kT}{4}\left[(\lambda^2 + 2/\lambda - 3) + B_1(1 + \lambda^2/\kappa) + 2B_2(1 + 1/\lambda\kappa) - \ln[(1 + B_1)(1 + B_2)^2(1 + \lambda^2 B_1/\kappa)(1 + B_2/\lambda\kappa)]\right] \quad (12)$$

$$B_1 = \kappa^2(\lambda^2 - 1)/(\lambda^2 + \kappa)^2 \quad B_2 = \kappa^2(1/\lambda - 1)/(1/\lambda + \kappa)^2$$

When $\kappa = 0$, the entanglements are not felt, and eq 12 reduces to the phantom network result. As κ approaches infinity, the junctions are held fixed relative to the macroscopic deformation, and the affine model is recovered. For intermediate values of κ the nonisotropic deformation dependence of the constraint potential leads to nonlinearity in the stress/strain behavior expressed in the Mooney−Rivlin form. For intermediate values of κ the uniaxial stress of a nonreacting network can be computed from eq 12 using $\sigma = \lambda\partial W/\partial\lambda$. This stress can then be used with the independent network hypothesis in eq 7 to calculate λ_s and the permanent set. It should be emphasized that the constrained junction model assumes that entanglements only affect the network junctions.

3.4. Slip-Tube Model. To describe the effects of entanglements along the chain backbones, various tube models[36−39] have been employed in the literature. In these models the effect of the entanglements is spread across the entire chain. In effect, a harmonic potential couples each chain segment to a background, elastic continuum. Rubinstein and Panyukov[26] developed a *slip-tube* model incorporating entanglement constraints that are able to slide along the chain backbone. For uniaxial deformation, they provided an analytic fit for the Mooney stress σ^*, valid for moderate strains

$$\sigma^* \equiv \frac{\sigma}{(\lambda^2 - 1/\lambda)} = G_c + \frac{G_e}{0.74\lambda + 0.61\lambda^{-1/2} - 0.35} \quad (13)$$

In eq 13, G_e is the shear modulus due to trapped entanglements

$$G_e \equiv \nu_e kT \quad (14)$$

G_e is directly measurable in a laboratory experiment or MD simulation. By contrast the number of chains/volume due to entanglements ν_e is a derived quantity that depends on the particular theory used to relate ν_e to G_e. In this investigation, eq 13 serves as our definition of ν_e. Combining the independent network hypothesis from eq 7 with eq 13 leads to

$$(\lambda_s^2 - \lambda_s^{-1})\left(1 + \frac{\nu_e/(\nu_1 - \nu_{gel})\alpha}{0.74\lambda_s + 0.61\lambda_s^{-1/2} - 0.35}\right) + \left(\frac{\lambda_s^2}{\lambda_2^2} - \frac{\lambda_2}{\lambda_s}\right)\frac{\nu_2}{\nu_1 - \nu_{gel}} = 0 \quad (15)$$

Equation 15 can be solved numerically to find the state-of-ease leading to the permanent set. Note that we have taken the entanglement contribution due to the stage 2 network to be negligible. The validity of this assumption will be addressed later in this paper.

3.5. Double-Tube Model. The double-tube model, developed by Everaers and co-workers,[27,28] models the different strain dependence of cross-link and entanglement confinement along strands and predicts an anisotropic, nonaffinely deforming tube. The double-tube model does not allow for slipping. The uniaxial stress predicted by the double-tube model is given by

$$\sigma = (\lambda^2 - 1)\left(\frac{2G_e^2\lambda^{-2} + G_c^2}{\sqrt{4G_e^2\lambda^{-2} + G_c^2}}\right) + (1 - \lambda^{-1})\left(\frac{2G_e^2\lambda + G_c^2}{\sqrt{4G_e^2\lambda + G_c^2}}\right) \quad (16)$$

In eq 16 the chemical and entanglement shear moduli have a similar interpretation as with the slip-tube model. As before we employ the independent network hypothesis in eq 7. Using eq 16 for the uniaxial stress we obtain the following expression for the determination of λ_s

$$(\lambda_s^2 - 1)\left(\frac{2\lambda_s^{-2}(\nu_e/(\nu_1 - \nu_{gel})\alpha)^2 + 1}{\sqrt{4\lambda_s^{-2}(\nu_e/\nu_1\alpha)^2 + 1}}\right) + (1 - \lambda_s^{-1})\left(\frac{2\lambda_s(\nu_e/(\nu_1 - \nu_{gel})\alpha)^2 + 1}{\sqrt{4\lambda_s(\nu_e/\nu_1\alpha)^2 + 1}}\right) + \left(\frac{\lambda_s^2}{\lambda_2^2} - \frac{\lambda_2}{\lambda_s}\right)\frac{\nu_2}{\nu_1 - \nu_{gel}} = 0 \quad (17)$$

As in the case of the slip-tube model, we also assume that the entanglement contribution to the stress is unaffected by the additional stage 2 cross-links.

4. Discussion

It can be seen from eq 10 for the affine and phantom models that the state-of-ease and permanent set depend on only two parameters: the stage 2 extension ratio λ_2 and the ratio of the number of second to first stage cross-links beyond the gel point $\nu_2/(\nu_1 - \nu_{gel})$. The constrained junction model prediction in eq 12 involves the additional parameter κ describing the coupling between the entanglements and the network junctions. Here we will compare the constrained junction model with MD simulations for κ values intermediate between the phantom and the affine models. The slip-tube (eq 15) and double-tube models (eq 17) both require knowledge of the entanglement spacing ν_e and the factor α from eq 9 relating the shear modulus to the number of chemical cross-links. In the present investigation, we have extracted these two parameters from MD simulation set A.

In Figure 8 we plot the Mooney stress obtained from the MD simulation set A as a function of the cross-link density relative to the gel point at three different extension ratios. The stress σ_0^* extrapolated to the gel point corresponds to an apparent entanglement shear modulus G_e. Not surprisingly, we find that σ_0^* is different for each extension ratio. Uniaxial stress is known to be a more complex function of strain than given in the neo-Hookean form in eq 8, particularly at large strains. However, we expect that in the limit of small strains $\lambda \rightarrow 1$ we should recover linear elastic behavior and that the entanglement shear

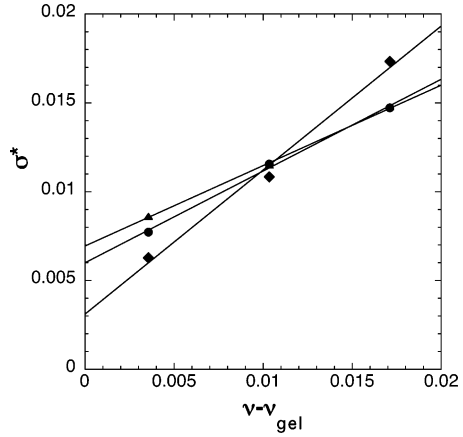

Figure 8. Reduced stress $\sigma^* = \sigma/(\lambda^2 - 1/\lambda)$ in a single-stage network as a function of cross-link density, $\nu - \nu_{gel}$, for various strains for simulations A. Results are from networks prepared from MD simulation set A: $\lambda = 1.5$ (triangles), $\lambda = 2.0$ (circles), and $\lambda = 4$ (diamonds). Lines are best fits. The extrapolated intercepts correspond to the entanglement stress.

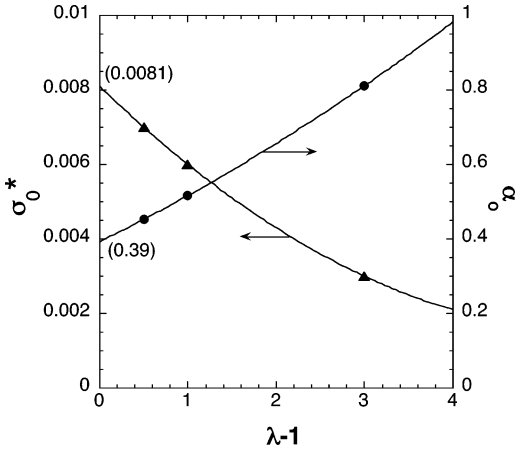

Figure 9. Estimation of the shear modulus G_e due to entanglements and the chemical cross-link density prefactor α of the shear modulus. The data from Figure 8 is extrapolated to $\lambda = 1$. Triangles represent the intercepts σ_0^* (values on the left axis), and the circles are the slopes α_0 from the previous figure (right axis). Extrapolations G_e and α are shown in parentheses.

modulus can be inferred from

$$G_e = \lim_{\lambda \to 1} \sigma_0^*$$

In Figure 9, we extrapolated the Mooney stress to zero strain from which we conclude $G_e = 0.0081\epsilon/\sigma_{LJ}^3$. From the definition of the entanglement spacing in eq 14 we infer that $\nu_e = 0.0081/\sigma_{LJ}^3$ for our bead−spring network. This corresponds to a degree of polymerization between entanglements of $N_e = \rho\sigma_{LJ}^3/0.0081 = 105$. This entanglement spacing is consistent with estimates of Everaers et al.[40] based on the plateau modulus from melt simulations. Since the entanglement spacing should be independent of chain length for long chains, we use the same value ν_e in comparing to both simulation sets A and B in this paper.

Using eq 9, we estimate the parameter α by first obtaining the slopes of the curves in Figure 8 at different extension ratios. These slopes were then extrapolated to zero strain as shown in Figure 9 leading to $\alpha = 0.39$ for networks prepared in simulation set A. This value of α is reasonable when compared to $\alpha = 0.5$ for the phantom model. Network imperfections and elastically ineffective chains will tend to reduce the equilibrium shear modulus. Although there could be small differences in α between simulations A and B owing to differences in network preparation, we neglect these differences and take α to be the same for both networks.

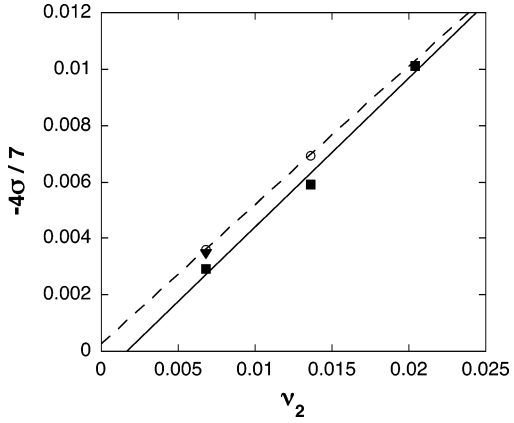

Figure 10. Reduced stress $\sigma/(\lambda^2/\lambda_2^2 - \lambda_2/\lambda) = -4\sigma/7$ from MD simulation set A for a two-stage network as a function of the second stage cross-link density, ν_2 for various values of ν_1. The σ values plotted were obtained after returning the stage two network from $\lambda_2 = 2$ to its original extension ratio $\lambda = 1$. Filled squares with the solid line represent $(\nu_1 - \nu_{gel}) = 0.00354/\sigma_{LJ}^3$, open circles with the dashed line represent $(\nu_1 - \nu_{gel}) = 0.0103/\sigma_{LJ}^3$, and the filled triangle represents a system with $(\nu_1 - \nu_{gel}) = 0.0171/\sigma_{LJ}^3$. Note that the curves extrapolate to $\sigma \approx 0$ when $\nu_2 \to 0$.

In section 3, we assumed that entanglements were only trapped by the first stage cross-links. To test this assumption, we compressed a series of two-stage networks back to their original length $\lambda = 1$. This strain state is the state-of-ease for the stage 1 cross-links and their entanglements. Any measured stress will be due to stage 2 cross-links and their associated entanglements. In Figure 10, we plot this stress as a function of the stage 2 network chain density ν_2. It can be seen from Figure 10 that the stress is approximately zero in the limit $\nu_2 \to 0$. This would not be the case if there were an additional entanglement contribution when the stage 2 cross-links are introduced. This observation justifies the form of eqs 15 and 17 for the state-of-ease in the slip-tube and double-tube models. In these equations, the only contribution from the entanglements is contained in the stage 1 term.

The states-of-ease and permanent set results are reported in Table 1 for MD simulation set A for various combinations of stage 1 and stage 2 network chain densities. λ_s was extracted from the MD simulations from interpolation as illustrated in Figure 3. The stage 2 deformation ratio was fixed at $\lambda_2 = 2$ for all cases studied in networks prepared in simulation set A. Permanent set results are shown in Table 2 for MD simulation set B for extension ratios of $\lambda_2 = 2$ and 4. Besides the method of introducing cross-links discussed above, the main difference between networks A and B is that the primary chain length is larger in the B simulations. Note in particular that the measured states-of-ease λ_s are close to unity in both sets of data in Tables 1 and 2 for $\nu_2 = 0$. This indicates that most of the viscoelasticity had relaxed and we achieved conditions close to equilibrium.

We now compare the permanent set obtained from simulation set A with theoretical predictions from the various models discussed in section 3. In Figures 11−13 we plotted the simulation results from Table 1 for the A networks. These networks were cross-linked to the three different levels ν_1 in the unstrained state as indicated in the figure. The simulated permanent set is plotted as a function of the ratio $\nu_2/(\nu_1 - \nu_{gel})$ as the points in these figures. The stage 2 cross-links were all introduced at a uniaxial extension ratio $\lambda_2 = 2$.

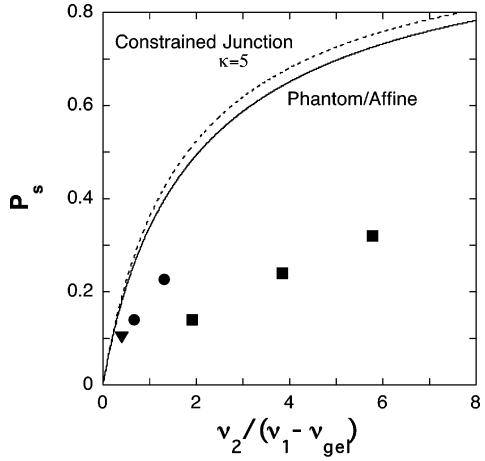

Figure 11. Permanent set results from MD simulations A compared with theoretical predictions from the classical (affine and phantom) model and the constrained junction model with $\kappa = 5.0$. Higher and lower values for κ bring the predictions closer to that of the classical (affine and phantom) models. Filled squares represent simulations with $\nu_1 - \nu_{gel} = 0.00354/\sigma_{LJ}^3$, circles $0.0103/\sigma_{LJ}^3$, and the filled triangle $0.0171/\sigma_{LJ}^3$.

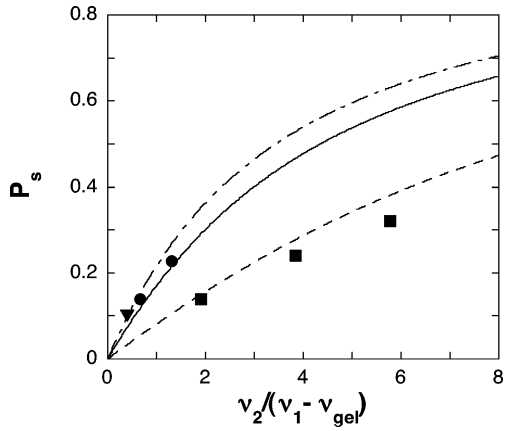

Figure 12. Permanent set results from MD simulations A compared with theoretical predictions from the slip-tube model. Filled squares (simulations) and the dashed line (theoretical) correspond to $\nu_1 - \nu_{gel} = 0.00354/\sigma_{LJ}^3$, circles and the solid line correspond to $0.0103/\sigma_{LJ}^3$, and the triangle and the dash−dotted line correspond to $0.0171/\sigma_{LJ}^3$.

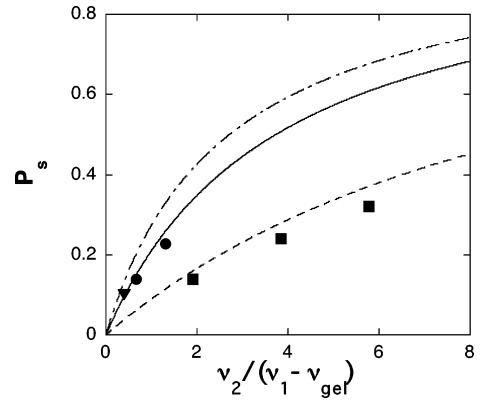

Figure 13. Permanent set results from MD simulations A compared with predictions from the double-tube model. Filled squares (simulations) and the dashed line (theoretical) correspond to $\nu_1 - \nu_{gel} = 0.00354/\sigma_{LJ}^3$, circles and the solid line correspond to $0.0103/\sigma_{LJ}^3$, and the triangle and the dash−dotted line correspond to $0.0171/\sigma_{LJ}^3$.

In Figure 11 we see a comparison between simulation and the affine and phantom model predictions obtained from eq 11. Also plotted in Figure 11 are the permanent set predictions for the constrained junction model inferred from eq 12 with the coupling parameter $\kappa = 5$. Note that the constrained junction model yields results that are very close to the affine/phantom predictions. Over the range of $\nu_2/(\nu_1 - \nu_{gel})$ shown in Figure 11, the differences in permanent set between the constrained junction and the affine/phantom models is maximized for $\kappa \approx 5$. Decreasing (increasing) κ moves the constrained junction model predictions closer to the phantom (affine) predictions. It can be seen from Figure 11 that the affine, phantom, and constrained junction models greatly overpredict the permanent set relative to the simulations. These observations are consistent with our earlier investigation.[15] It is also apparent from the points in Figure 11 that the permanent set depends explicitly on ν_1. It is clear from eqs 11 and 12 that both the affine/phantom and the constrained junction models depend only on the ratio $\nu_2/(\nu_1 - \nu_{gel})$.

A common feature of the constrained junction, affine, and phantom models is that they are *junction* models in the sense that only the positions of the network junctions are relevant in the calculation of the strain energy. The effects of entanglements are either absent or affect only the network junctions. We now turn our attention to *tube* models that explicitly account for the effects of entanglements on all the sites along the backbones of the network chains. In Figure 12, we show a comparison between simulation of the A networks and the slip-tube model. The permanent set was calculated from eq 15 using the ν_e and α values determined above. We now observe that theory, like the simulations, yields different permanent sets for different levels of first stage cross-links. This is because the slip-tube model in eq 15 depends on the entanglement spacing through the ratio $\nu_e/(\nu_1 - \nu_{gel})\alpha$. It can be seen that the agreement between the slip-tube model and the simulations is very good. In Figure 13 we show a similar comparison between the A network simulations and the double-tube model obtained from eq 17. As can be seen in the figure, the double-tube model is also in very good agreement with the simulations.

We now examine the permanent sets found from simulation set B. In Figures 14a and 14b we plot the network B permanent sets from Table 2 for $\lambda_2 = 2$ and 4. All the B network simulations were carried out for a single density of stage 1 cross-links. Theoretical permanent set predictions for all models are shown along with the simulations in these figures. As seen with the network A simulations, the slip-tube and double-tube models are also in very good agreement with the B network simulations, while the junction models overestimate the permanent set. On the basis of MD simulations on both A and B networks, we conclude that entanglements play a crucial role in determining the permanent set of polymer networks.

Since all our conclusions are based on the use of the independent network hypothesis, in combination with the various theoretical models, a brief discussion of the applicability of this hypothesis for each model is instructive. In previous studies, the independent network hypothesis was demonstrated to agree well with MD simulations of cross-linking in uniaxially strained states.[15] In fact, while the affine[8] and phantom[9] models have been proven to obey the independent network hypothesis for Gaussian chains, those models did not match our simulation results.

Comparable theoretical calculations have not as yet been carried out for the constrained junction or tube models. However, since the constrained junction model reduces to the affine and phantom models in the two limits of κ, it seems likely that this model would obey the independent network model for intermediate values of κ. The slip-tube model has been formulated

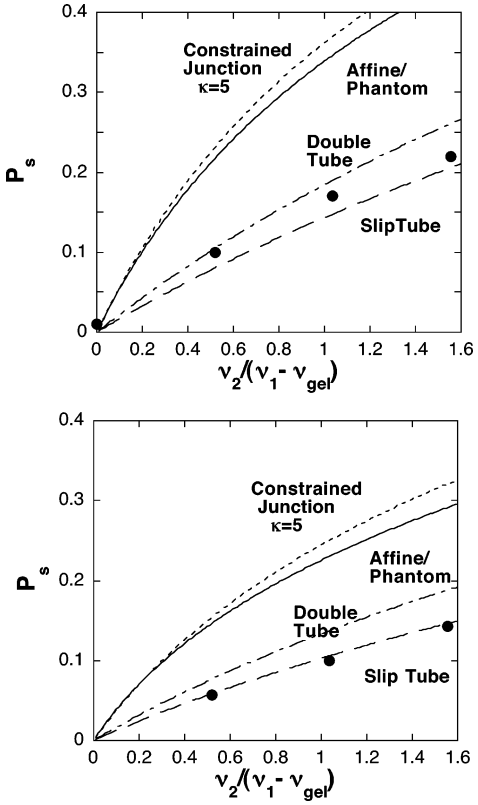

Figure 14. Permanent set results (circles) from MD simulations B compared with theoretical predictions from the models indicated: (upper panel) $\lambda_2 = 2$, (lower panel) $\lambda_2 = 4$.

as the simple sum of the entanglement and chemical cross-link contributions (eq 13), and we speculate that it would obey the independent network hypothesis as well. In the case of the double-tube model, we see from eq 16 that the entanglement and chemical cross-link density are coupled. As a result, the double-tube model may not reduce to the independent network hypothesis but instead to a more general form. However, our simulations showed that only first stage cross-linking traps entanglements indicating that, to a good approximation, only entanglements as they affect the first network need be considered. Future theoretical investigations on tube models for two-stage networks are needed to address these questions.

5. Conclusions

In this investigation we performed MD simulations of cross-linking bead−spring polymer networks. From these simulations, we deduced the states-of-ease and permanent sets for a range of cross-linking and uniaxial strain histories. Comparing these simulations with various theoretical models of rubber elasticity, we observed that junction models (affine, phantom, constrained junction) predict permanents sets much larger than those observed in the simulations. By contrast, tube models (slip-tube, double-tube) that explicitly account for entanglement effects on the fluctuations of network chains were in very good agreement with simulation. Thus, entanglements play a crucial role in determining the permanent set of polymer networks. We also found that trapped entanglements only affect the stress from first stage network; adding additional stage 2 cross-links in the strained state does not require any additional entanglement contribution. We emphasize that our combination of constitutive equations from tube models of rubber elasticity with the independent network hypothesis, while empirically successful, is not based on molecular theory. The development of such a theory, which simultaneously describes the macroscopic stresses and the microscopic deformations remains a challenge.

Besides analyzing the macroscopic elastic behavior, we have presented (for the first time) data on the length-scale-dependent microscopic deformations in postcured networks. The microscopic signatures of a finite permanent set are locally isotropic chain conformations for $1 < \lambda = \lambda_s$ and locally *compressed* chains in globally *elongated* samples with $1 < \lambda < \lambda_s$. Independently of postcuring, the networks deform affinely on larger scales. Our data suggest that these effects should be clearly observable in neutron scattering experiments with suitably labeled networks. Such studies would complement the present results for model networks and would be valuable in guiding and gauging theoretical efforts on chemically reacting networks.

The simulations performed in this study involved networks undergoing only cross-linking reactions. The effect of scission reactions, where cross-links formed at earlier stages are removed, was beyond the scope of this investigation. We know from the work of Flory[8] on affine networks and Fricker[9] on phantom networks that the independent network hypothesis breaks down in this case. Cross-links formed at later stages take over the roles of earlier stage cross-links upon removal of the earlier stage cross-links. Combined cross-linking and scission of bead−spring networks will be the subject of a future investigation.

Acknowledgment. Sandia is a multiprogram laboratory operated by Sandia Corporation, a Lockheed Martin Company, for the United States Department of Energy's National Nuclear Security Administration under Contract No. DE-AC04-94-AL85000. The authors acknowledge Aidan Thompson whose modified LAMMPS code was used for the simulation set A presented here.

References and Notes

(1) Curro, J. G.; Salazar, E. A. *J. Appl. Polym Sci.* **1975**, *19*, 2571. Curro, J. G.; Salazar, E. A. *Rubber Chem. Technol.* **1977**, *50*, 895.
(2) Salazar, E. A.; Curro, J. G.; Gillen, K. T. *J. Appl. Polym Sci.* **1977**, *21*, 1597.
(3) Tobolsky, A. V. *Properties and Structure of Polymers*; Wiley: New York, 1960.
(4) Tobolsky, A. V.; Prettyman, I. B.; Dillon, J. H. *J. Appl. Phys.* **1944**, *15*, 380.
(5) Andrews, R. D.; Tobolsky, A. V.; Hanson, E. E. *J. Appl. Phys.* **1946**, *17*, 352.
(6) Berry, J. P.; Scanlan, J.; Watson, W. F. *Trans. Faraday Soc.* **1956**, *52*, 1137.
(7) Scanlan, J.; Watson, W. F. *Trans. Faraday Soc.* **1958**, *54*, 740.
(8) Flory, P. J. *Trans. Faraday Soc.* **1960**, *56*, 722.
(9) Fricker, H. S. *Proc. R. Soc. London, Ser. A* **1973**, *335*, 267.
(10) Huntley, H. E.; Wineman, A. S.; Rajagopal, K. R. *IMA J. Appl. Math.* **1997**, *59*, 309.
(11) Wineman, A. S.; Rajagopal, K. R. *Arch. Mech.* **1990**, *42*, 53.
(12) Rajagopal, K. R.; Wineman, A. S. *Int. J. Plast.* **1992**, *8*, 385.
(13) Mott, P. H.; Roland, C. M. *Macromolecules* **2000**, *33*, 4132.
(14) Santangelo, P. G.; Roland, C. M. *Rubber Chem. Technol.* **2003**, *76*, 892.
(15) Rottach, D. R.; Curro, J. G.; Grest, G. S.; Thompson, A. P. *Macromolecules* **2004**, 37, 5468.
(16) Everaers, R.; Kremer, K. *Macromolecules* **1995**, *28*, 7291. Everaers, R.; Kremer, K. *Phys. Rev E* **1996**, *53*, R37.
(17) For a review, see: Everaers, R. *New J. Phys.* **1999**, *1*, 12.1.
(18) Svaneborg, C.; Grest, G. S.; Everaers, R. *Phys. Rev. Lett.* **2004**, *93*, 257801. Svaneborg, C.; Grest, G. S.; Everaers, R. *Polymer* **2005**, *46*, 4283.
(19) Grest, G. S.; Kremer, K. *J. Phys. Fr.* **1990**, *51*, 2829. Grest, G. S.; Kremer, K. *Macromolecules* **1990**, *23*, 4994.
(20) Duering, E. R.; Kremer, K.; Grest, G. S. *Macromolecules* **1993**, *26*, 3241. Duering, E. R.; Kremer, K.; Grest, G. S. *J. Chem. Phys.***1994**, *101*, 8169.
(21) Grest, G. S.; Kremer, K.; Duering, E. R. *Physica A* **1993**, *194*, 330.
(22) Treloar, L. R. G. *The Physics of Rubber Elasticity*; Clarendon Press: Oxford, 1975.

(23) James, H. M.; Guth, E. *J. Chem. Phys.* **1943**, *11*, 455.
(24) Ronca, G.; Allegra, G. *J. Chem. Phys.* **1975**, *63*, 4990.
(25) Erman, B.; Flory, P. J. *J. Chem. Phys.* **1978**, *68*, 5363.
(26) Rubinstein, M.; Panyukov, S. *Macromolecules* **2002**, *35*, 6670.
(27) Everaers, R. *Eur. Phys. J. B* **1998**, *4*, 341.
(28) Mergell, B.; Everaers, R. *Macromolecules* **2001**, *34*, 5675.
(29) Plimpton, S. *J. Comput. Phys.* **1995**, *117*, 1.
(30) Westermann, S.; Pyckhout-Hintzen, W.; Richter, D.; Straube, E.; Egelhaaf, S.; May, R. *Macromolecules* **2001**, *34*, 2186.
(31) Svaneborg, C.; Grest, G. S.; Everaers, R. *Europhys. Lett.* **2005**, *72*, 760.
(32) Wall, F. T.; Flory, P. J. *J. Chem. Phys.* **1952**, *19*, 1435.
(33) Flory, P. J. *J. Chem. Phys.* **1977**, *66*, 5720.
(34) Erman, B.; Flory, P. J. *Macromolecules* **1982**, 15, 806.
(35) Erman, B.; Kloczkowski, A.; Mark, J. E.; Flory, P. J. *Macromolecules* **1989**, *22*, 1432.
(36) Heinrich, G.; Straube, E. *Acta Polym.* **1983**, *34*, 589. Heinrich, G.; Straube, E. *Acta Polym.* **1984**, *35*, 115.
(37) Rubinstein, M.; Panyukov, S. V. *Macromolecules* **1997**, *30*, 8036.
(38) Ball, R. C.; Doi, M. ; Edwards, S. F.; Warner, M. *Polymer* **1981**, *22*, 1010.
(39) Edwards, S. F.; Vilgis, T. *Polymer* **1986**, *27*, 483.
(40) Everaers. R.; Sukumaran, S. K.; Grest, G. S.; Svaneborg, C.; Sivasubramanian, A.; Kremer, K. *Science* **2004**, *303*, 823. Sukumaran, S. K.; Grest, G. S.; Kremer, K.; Everaers, R. *J. Polym. Sci., Part B: Polym. Phys.* **2005**, *43*, 917.

MA060767X